applied optics

Direct absorption spectroscopy baseline fitting for blended absorption features

Joshua M. Weisberger,[1] Joseph P. Richter,[1] Ronald A. Parker,[2] and Paul E. DesJardin[1,*]

[1]Mechanical and Aerospace Engineering, University at Buffalo, Buffalo, New York 14260, USA
[2]CUBRC, Buffalo, New York 14225, USA
*Corresponding author: ped3@buffalo.edu

Received 25 June 2018; revised 31 August 2018; accepted 26 September 2018; posted 27 September 2018 (Doc. ID 335877); published 18 October 2018

A method for determining the gas concentration from blended absorption features using direct absorption spectroscopy is developed. Blended spectra occur when multiple absorption lines are in close proximity in a laser scan and/or when pressures begin to increase. The blended-feature baseline fitting method estimates the baseline by coupling measured data with simulated fractional transmission at the peaks between absorption features. The method is first validated with synthetically created data. The method is then demonstrated using the absorption lines of CO_2(P41e, P42f, P34e, P43e) and H_2O in the $\nu_1 + \nu_3$ combination band (3683.5 cm^{-1} to 3686.5 cm^{-1}) in a heated static test cell. Results from the fitting method and wavelength modulation spectroscopy measurements agree within 1%. The method is finally applied to measurements of flue gas emissions from a practical combustion system (wood boiler) and compared to measurements from a hand-held gas analyzer. The mean percent difference of the blended-feature baseline fitting and the wavelength modulation spectroscopy is 2.8% and 5.8% for X_{CO_2} and X_{H_2O}, respectively, indicating that this method of direct absorption data analysis can be used for spectra with moderate feature blending, which is useful for scan ranges with multiple closely spaced absorption lines and moderate pressures.

OCIS codes: (300.6260) Spectroscopy, diode lasers; (280.1740) Combustion diagnostics; (300.1030) Absorption.

https://doi.org/10.1364/AO.57.009086

1. INTRODUCTION

The measurement of CO_2 and H_2O in combustion environments is important for monitoring the completeness of combustion processes. The absorption features of typical combustion products generally fall in the infrared spectrum due to their ro-vibrational energy transitions. Tunable diode laser absorption spectroscopy (TDLAS) provides an accurate, fast, nonintrusive diagnostic to probe these absorption features.

Scanned wavelength direct absorption spectroscopy (DAS) has been used extensively for combustion product monitoring [1–3]. The DAS technique allows for low-cost detectors and data acquisition systems, intuitive interpretation of the raw data, and relatively simple data processing and analysis. To obtain gas properties from DAS data, a nonabsorbing baseline is needed during the analysis process, which is defined as the signal detected when the laser is not absorbed by any gases along its beam path. Low pressure or isolated line measurements have been performed for both H_2O [4–12] and CO_2 [4,6,10,13–23].

However, when absorption lines are closely spaced in a wavenumber scan range or the measurement pressure increases, the features become blended and a clear nonabsorbing baseline is sometimes not available for the analysis. Probing multiple lines/species is desirable to gather as much information as possible, and multiple-laser systems have been used at an increase in cost of the total setup [4,6,9,10,13,20,24,25]. High pressures cannot always be avoided in combustion applications, and some measurements have been made in these environments using much wider scan ranges to probe an entire P or R branch [8,23,26,27].

Most commonly, the baseline is defined by directly fitting a low-order polynomial to the nonabsorbing data in the wings of the feature. The gas properties are then determined by iteratively finding the best fit of the baseline plus line shape function to the raw absorption data. This works well for completely isolated features. Other methods use a reference signal for the baseline, which is scaled such that the signals match in magnitude outside the regions of the absorption peaks. In this way, actual recorded data from the laser are used as the baseline signal. This proves difficult in cases where the baseline shape does not stay the same, such as when etaloning causes the fringes to move during a run.

One approach to circumvent the problems of blended features is the use of wavelength modulation spectroscopy

(WMS) [28–41]. Although minimal changes are needed to convert from a DAS to a WMS setup, the detectors and data acquisition systems require much higher sampling rates, which can significantly increase costs. This technique is useful because the features can be blended and a nonabsorbing baseline is not required, while the downsides are that the results are not immediately intuitive and the data processing is more intensive. In WMS, the absorption information is shifted to higher frequencies, resulting in increased signal-to-noise, and isolation from $1/f$ laser noise and low-frequency undulations. In this study, the $1f$-normalized $2f$ harmonic signal is used to determine gas concentrations [36].

To bridge the gap between isolated-feature DAS and WMS measurements, a blended-feature baseline fitting method (BFBL) is developed in this study. It uses an efficient iterative lookup table (LUT) approach, where the baseline is estimated by coupling measured data with simulated fractional transmission at the peaks between absorption features. The coupling is required when the entire laser wavenumber scan range is fully blended, but also works for isolated features. In this approach, a functionalized curve fitting of the baseline is iterated with the regression analysis of the absorption features.

The rest of this study is organized as follows. The laser diagnostic setup is first described in Section 2, including the setup for both the DAS and WMS measurements and the differences between the two. In Section 3, the BFBL fitting technique is derived. Synthetic spectra are then used to test the baseline fitting technique to make sure it is self-consistent in Section 4.A. In Section 4.B, a heated static test cell ($L = 15.24$ cm, $P = 1$ atm) is used to validate the fitting technique with a known gas concentration and WMS measurements. In Section 4.C, the baseline fitting method is applied to analyze the combustion product flue gases from a wood-fired two-stage hydronic heater, and Section 5 summarizes the conclusions of this study.

2. LASER DIAGNOSTIC SETUP

The laser measurement operates as a pitch-catch system [Fig. 1(a)], where the laser signal is generated on one side of the gases of interest, pitched through the absorbing gases, and caught on the other side to measure the fractional absorption. Both the pitch and catch sides are independently housed inside nitrogen (N_2)-purged boxes to avoid absorption from the CO_2 and H_2O present in the lab atmosphere.

The wavenumber-scanning laser (L) first splits at a 50-50 beam splitter (BS), where half of the intensity passes through a solid germanium etalon (E) with a free spectral range (FSR) of 0.0235 cm^{-1} and into a Thorlabs PDA10PT detector (1.6 MHz bandwidth, 1 mm^2 active area). The data are collected on channel 3 (CH3) and provide a time-to-wavenumber transformation of the measured data. The other half of the beam's intensity passes through the first BS and is split again using a second identical BS. Half of this beam is directed to a KISDP-1-J1/DC Kolmar detector (15 MHz bandwidth, 1 mm^2 active area), for use as a nonabsorbing laser signal and is collected on channel 2 (CH2). The rest of the beam passes through the second BS, through the test gas of interest,

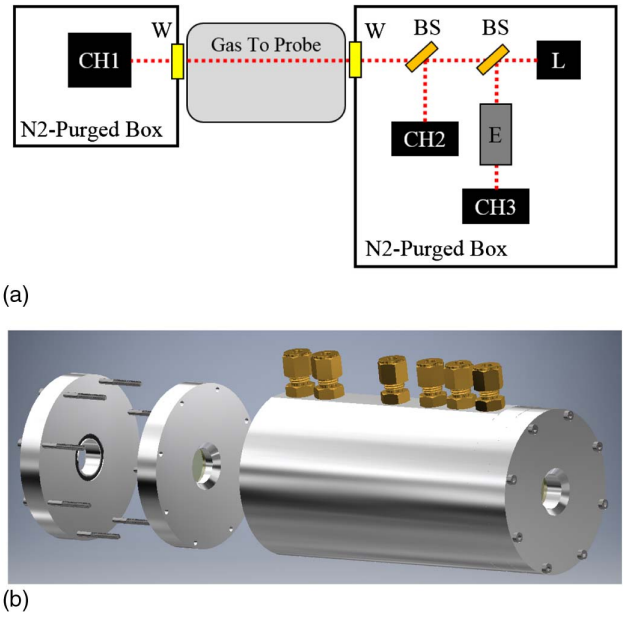

Fig. 1. (a) Laser pitch-catch setup schematic and (b) static heated test cell CAD model.

and into the catch box. The beam is incident on another identical Kolmar detector for use as the absorbing laser signal and is collected on channel 1 (CH1). Sapphire-wedged windows (W) with an antireflection coating are used to isolate the pitch and catch boxes from the laboratory environment and to make sure the boxes remain purged. CH1 and CH3 are used for the DAS analysis, while all three channels are used for the WMS analysis. Any system with appropriate absorbing gases can be placed between the pitch and catch boxes of the laser system. For example, a heated test cell is used in this study to validate the baseline fitting method [Fig. 1(b)].

A NanoPlus distributed feedback tunable diode laser probes the CO_2(P41e, P42f, P34e, P43e) and H_2O lines in the $\nu_1 + \nu_3$ combination band, scanning between 3683.5 cm^{-1} and 3686.5 cm^{-1} [6,7,15,18,24,42]. A Lightwave 6100 Combination Laser Diode Driver and Temperature Controller (LDD-TEC) is used to control the laser current and temperature. To scan over the wavenumber range, the injection current is tuned by applying a modulated voltage from an AFG3051C Tektronix Arbitrary/Function Generator. To center the laser at 3685 cm^{-1}, the temperature and injection current are set to 34.5°C and 155 mA, respectively.

For these measurements, a waveform including both a WMS ramp and a DAS ramp (in succession) is used, as seen in Fig. 2. The slow-scan ramp frequency of the waveform is $f_R = 40$ Hz, while the modulation frequency for the WMS ramp shown in the figure is $f_M = 1$ kHz (in order to easily see the modulation); when actually performing the measurement, the modulation frequency is $f_M = 10$ kHz. While the DAS and WMS measurements are not exactly coincident in time, the difference of 25 ms between the WMS and DAS absorption features is fast enough compared to transients in all flows analyzed in this study. The function used to modulate the injection current to the laser for the WMS portion of the ramp is

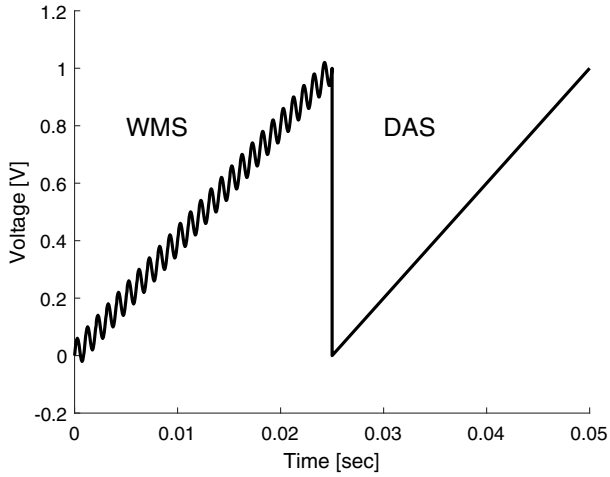

Fig. 2. Function generator WMS and DAS ramps in succession.

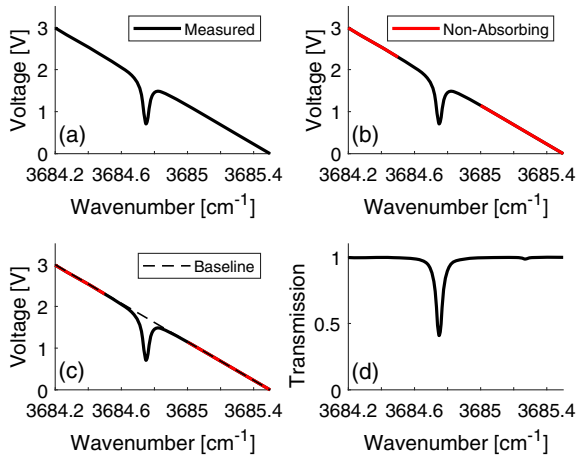

Fig. 3. Simple baseline fitting for isolated features at low pressures.

$$\nu(t) = \nu_R(t) + a_M \sin(2\pi f_M t), \tag{1}$$

where $\nu_R(t)$ is the DAS ramp voltage and a_M is the modulation depth [cm^{-1}]. The optimum modulation depth is related to the modulation index (m) and the FWHM ($\Delta\nu$) of the absorbing peak of interest. The optimum modulation index occurs when the maximum WMS signal is obtained, which for the second harmonic is when $m = 2.2$ [43]:

$$m = \frac{a_M}{\Delta\nu/2} = 2.2. \tag{2}$$

The optimum value of a_M depends on the width of the spectral features the laser is probing (through the $\Delta\nu$ term) and changes when the properties of the gases change. An appropriate value is chosen that is generally optimum over all the ranges of gas properties anticipated. The modulation depth used in this study is 0.18 cm^{-1} (6% of a 3 cm^{-1} laser scan range).

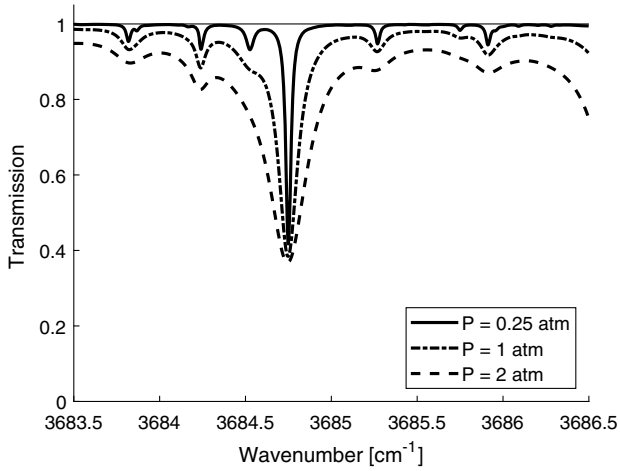

Fig. 4. Transmission spectra for varying absorbing path length pressure, $T = 422$ K, $L = 15.24$ cm, $X_{CO_2} = 0.05$, $X_{H_2O} = 0.05$.

3. BFBL FITTING

A. Motivation

When absorption features in the wavenumber scan range are sufficiently isolated, the baseline fitting is straightforward, as illustrated in Fig. 3. Regions on either side of the feature where no absorption is occurring are selected (b) and used to fit a nonabsorbing baseline (c). The final transmission curve is obtained by dividing the measured voltage by the baseline voltage (d).

When absorption lines are closely spaced and/or pressures are moderate-to-high, the isolated feature method can no longer be used. Figure 4 shows the absorption spectra for gas pressures of 0.25 atm, 1 atm, and 2 atm ($T = 422$ K, $L = 15.24$ cm, $X_{CO_2} = 0.05$, $X_{H_2O} = 0.5$). At low pressure, regions with no absorption are clearly visible (transmission equal to unity). When the pressure is increased, even to just 1 atm, there is no point in the wavenumber range where the transmission returns to unity. As the pressure is increased further, the problem becomes worse.

As an added difficulty, the baseline shown in Fig. 3(c) is linear, but this is not always the case, even when tuning the laser injection current linearly over the wavenumber range. A major source of baseline distortion is due to parallel-faced optics in the beam path, which cause a low-order waviness of the baseline (etaloning). These issues can generally be avoided by using wedged optics, but this is not always feasible, especially when the detectors have flat protective windows. Effects of parallel-faced optics in the beam path are shown in Fig. 5. Three voltage traces are shown for the same nominal conditions (T, P, L, X_{CO_2}, X_{H_2O}). The solid line shows the trace with no distortion, and the baseline can be easily represented by a low-order polynomial. The dashed and dash-dot data show voltage traces with significant etaloning present, and the baseline becomes more problematic to fit. None of the measured signals are the same, even though they are all measuring the same gas properties.

Both the blended nature of the overlapping absorption features and the baseline distortion from etaloning make the determination of the gas properties difficult, but are included in the analysis method detailed in this study.

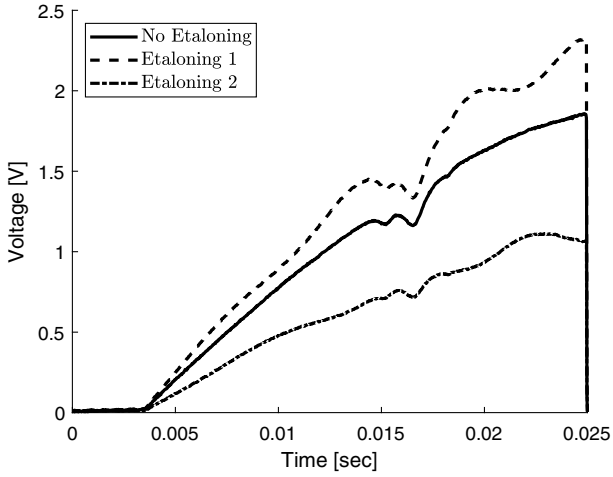

Fig. 5. Absorbing data detector traces for different orientations of a CaF_2 nonwedged window between laser and detector.

B. Line-by-Line Simulations

The absorption of monochromatic radiation through a weakly absorbing, homogeneous medium is governed by the Beer–Lambert law,

$$\tau = \frac{I}{I_0} = \exp(-k_\nu L), \tag{3}$$

where τ is the fractional transmission, I_0 is the incident intensity, I is the transmitted intensity, and the product of the spectral absorption coefficient and absorbing path length ($k_\nu L$) is the absorbance, α. The spectral absorption coefficient is given as

$$k_\nu = S_i(T) P X \phi_\nu, \tag{4}$$

where $S_i(T)$ is the temperature-dependent line strength, P is pressure, X is absorbing species mole fraction, and ϕ_ν is the spectral line shape function. Reference spectroscopic data at 296 K were obtained from the HITRAN 2016 database [44]. Care must be taken when using spectroscopic information from the database. The wavenumber region used in this study has been extensively researched, so confidence in the parameters is high. If a less-researched wavenumber range is to be used, fundamental measurements of the spectroscopic parameters will need to be performed. The line strength is not a function of line shape and can be scaled to temperatures other than the reference temperature using the following relation:

$$S_i(T) = S_i(T_0)\frac{Q(T_0)}{Q(T)}\left(\frac{T_0}{T}\right)\exp\left[\frac{-hcE''}{k}\left(\frac{1}{T}-\frac{1}{T_0}\right)\right] \times \left[1-\exp\left(\frac{-hc\nu}{kT}\right)\right]\left[1-\exp\left(\frac{-hc\nu}{kT_0}\right)\right]^{-1}. \tag{5}$$

A third-order polynomial is used to fit the total internal partition function (Q) from the given data in the HITRAN database. The spectral line shape is a function of multiple types of broadening mechanisms, with the two dominating forms in this study being Doppler broadening and collisional broadening. Both broadening FWHM values are comparable, so a Voigt line shape is needed to describe the convolution of the two line shapes. An approximate analytical model of the full frequency-space convolution can be used with good accuracy, reducing computational time of a full convolution calculation [45].

When simulating the HITRAN spectra for blended features, the wavenumber range used for the simulation must be much wider than the wavenumber scan range of the laser measurements to ensure that broad features from neighboring transitions are included in the simulation. The fundamental CO_2 P36e and P32e lines are in close proximity to the scan range, and care must be taken to extend the simulation range wide enough to include these broadened lines outside the region of interest. Extending the simulation range out by 5 cm^{-1} on both sides of the spectrum is sufficient to capture the influence of neighboring transitions. As pressure increases, this range must be extended further.

C. DAS Baseline Fitting

The BFBL fitting method is an iterative, coupled process between simulation LUTs and the measured data. The LUTs contain precomputed spectra for combinations of [X_{CO_2}, X_{H_2O}] at known values of P, L, and T. A flow chart of the process is shown in Fig. 6, and to demonstrate the procedure, Fig. 7 visualizes the flow chart steps for a single iteration. In each (i, j) iteration, the combination of appropriate X_{CO_2} and X_{H_2O} gives the simulated transmission (τ_S) versus wavenumber spectrum [black line in Fig. 7(a)]. The BFBL is functionally parameterized as

$$V_{BL}(\nu) = F(\nu, a_k(\nu_i^*, V_i^*)), \tag{6}$$

where ν is the same wavenumber range as the simulated spectrum and a_k are the fitting coefficients. The peak values of transmission between absorption features are selected at wavenumbers ν_i^*, three of which are shown in Fig. 7(a). Since τ_S does not return to unity at any point in the wavenumber range, the peak points are the closest it gets between absorption features. These points are used as anchors for the baseline because it is unknown where in voltage space the baseline is located.

The absorbing data from CH1 (measured voltage V_M versus t) is converted to wavenumber space using the etalon data (wavenumber ν versus t). The anchor points are defined at discrete wavenumber values (ν_i^*), and the corresponding

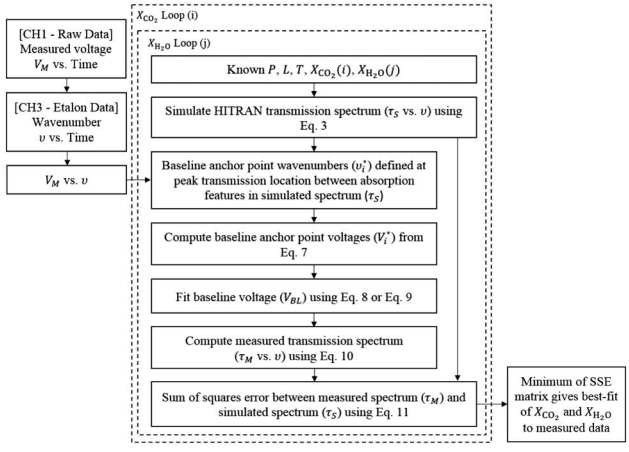

Fig. 6. Flow chart for DAS baseline fitting data analysis.

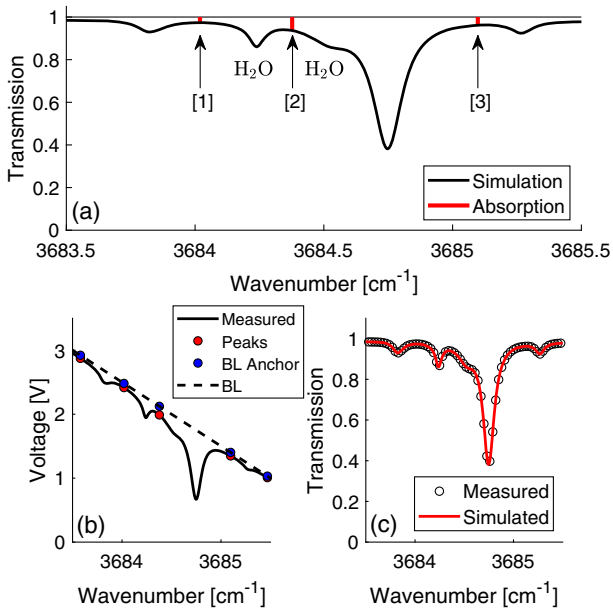

Fig. 7. Fitting procedure and data reduction for comparison between measured and simulated data, with (a) the simulated spectrum, (b) the measured data and baseline anchor points, and (c) the comparison between measured and simulated spectra.

voltage of the measured data at these wavenumbers ($V_M(\nu_i^*)$) is shown as red circles in Fig. 7(b). The baseline anchor voltage, V_i^*, is defined by

$$V_i^*(\nu_i^*) = \frac{V_M(\nu_i^*)}{\tau_S(\nu_i^*)}, \tag{7}$$

such that the transmission obtained from the measured data and these baseline points will return exactly the simulated transmission. The absorption from the simulations ($1 - \tau_S$) is shown as red lines in Fig. 7(a), and the values of $V_i^*(\nu_i^*)$ are shown as blue circles in Fig. 7(b).

The (ν_i^*, V_i^*) pairs are used to create the function $V_{BL}(\nu)$ over the entire wavenumber scan range by fitting the coefficients a_k of an appropriate function. The resulting baseline is shown in dashed black in Fig. 7(b). Two possible fitting functions are explored. The first is a polynomial fit,

$$V_{BL}(\nu) = \sum_{k=0}^{N} a_k \nu^k, \tag{8}$$

and the second is a Fourier series fit:

$$V_{BL}(\nu) = a_0 + \sum_{k=1}^{N} [a_k \cos(2\pi k f \nu) + b_k \sin(2\pi k f \nu)]. \tag{9}$$

A linear baseline fit corresponds to the limit when $N = 1$ for the polynomial fit. The frequency, f, in the Fourier fitting is the frequency of the slow-scan ramp (f_R), and the order of the harmonics is k. The measured data and the measured/simulated-coupled baseline are used to compute the measured transmission spectrum τ_M in the conventional way using

$$\tau_M(\nu) = \frac{V_M(\nu)}{V_{BL}(\nu)}. \tag{10}$$

A comparison of the measured (black circles) and simulated (solid red line) transmission spectra is shown in Fig. 7(c). The goodness-of-fit of the simulated and measured spectra is computed using a sum of squares error (SSE) over the entire wavenumber range. Weighting of different wavenumber regions (w_ν) is used to increase sensitivity of absorption features that have a smaller influence on the nonweighted SSE, such as the two H_2O features that appear near the fundamental CO_2 feature:

$$\mathrm{SSE}(i,j) = \sqrt{\sum_{\nu} w_\nu (\tau_M - \tau_S)^2}. \tag{11}$$

The best-fit values of both X_{CO_2} and X_{H_2O} are obtained simultaneously by identifying the minimum of the SSE matrix for all combinations. Tabulated LUTs are used to decrease computation time.

To increase the robustness of the fitting from noise inherent in the raw data, ranges about the anchor points are also considered. Individual anchor points at the peak transmission ($\nu_i^* = \nu_{i,\mathrm{peak}}^*$) were used in the previous methodology, but when noise in the raw data voltage increases, spurious baselines can occur due to the points being located anywhere between the maximum or minimum of the noise amplitude at that wavenumber. For these data traces, it is more robust to use the set of anchor points that includes wavenumber ranges centered at the peak transmission points ($\nu_i^* = \{\nu_{i,\mathrm{peak}}^* \pm d\nu\}$). These ranges are kept small, but effectively use the average of the noise in the wavenumber range to construct the baseline. While the values of $\nu_{i,\mathrm{peak}}^*$ can shift with changes in absorbing gas properties, the wavenumber location of these peaks is selected from each simulation's maximum locations between absorption features, so this shift is always inherently accounted for.

4. RESULTS AND DISCUSSION

A. Synthetic Data Analysis

Synthetic absorption data sets are first used to test the fitting algorithm subject to random noise and baseline etaloning. The parameters for all the following synthetic simulations are $P = 1$ atm, $L = 15.24$ cm, $T = 422$ K, $X_{CO_2} = 0.05$, and $X_{H_2O} = 0.07$. The transformation from time-space to wavenumber-space is already performed. Both random signal noise (Johnson noise) and baseline etaloning (Fig. 5) are introduced in the synthetic data to mimic actual data that might be taken.

1. Uncorrected Baseline Analysis

The uncorrected baseline is functionally parameterized as

$$V_{BL,u}(\nu) = F(\nu, a_k(\nu_i^*, V_{M,i})), \tag{12}$$

because $\tau_S(\nu_i^*) = 1$, and its effects are first explored using the results in Fig. 8. A synthetic V_M versus ν trace (solid black) has transmission peaks marked as blue circles in (a). Under the assumption that at the peak points the transmission returns to its nonabsorbing value of unity, the uncorrected baseline ($V_{BL,u}(\nu)$) is fit directly using the peak points.

The measured voltage is divided by the uncorrected baseline, resulting in the measured transmission spectrum, $\tau_M(\nu)$, shown in Fig. 8(b) with a dashed red line. The exact transmission spectrum (black line) was used to create the

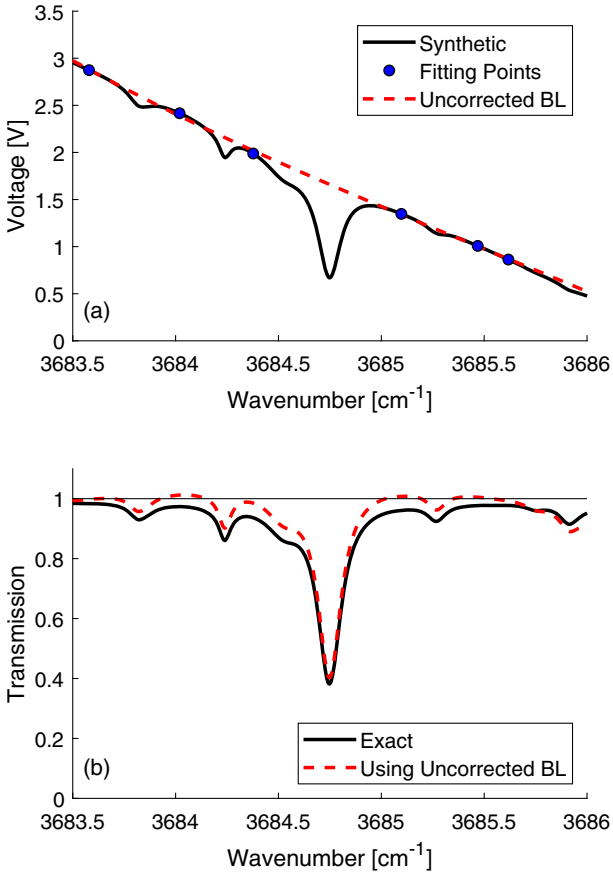

Fig. 8. Plots of (a) synthetic data trace with peak transmission fitting points and corresponding uncorrected baseline, and (b) comparison of exact transmission with measured spectrum assuming uncorrected baseline.

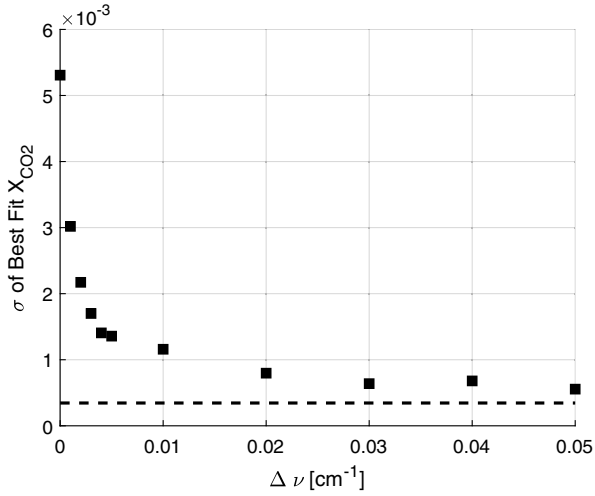

Fig. 9. Standard deviation of best fit CO_2 simulations for varying baseline anchor point wavenumber ranges. A wavenumber range of 0 cm^{-1} indicates fitting with single points.

synthetic data trace, and with an accurate baseline definition, the measured spectrum should return the exact simulation spectrum. The difference between the two spectra is due to the incorrect baseline specification, by assuming the peak values between absorption features in the measured data correspond to voltages when the beam is not being absorbed. With this assumption, the best-fit values of both X_{CO_2} and X_{H_2O} will be underpredicted. This assumption is only valid if no absorption takes place at the anchor wavenumbers, which is the case for the nonabsorbing region shown in Fig. 3(b).

2. Corrected Baseline: $\Delta\nu$ Range

As shown in Fig. 7, peak transmission points are used to define the baseline. However, noise in the raw data causes the fits using single points at the peaks to deviate significantly based on where in the noise voltage space the fitting point is located. To avoid this sensitivity, wavenumber ranges ($\Delta\nu$) about the peak transmission points are used to effectively take an average value of the noise in these ranges. The choice of wavenumber range to use are obtained from a plot of the standard deviation of the best-fit values for multiple simulations of the synthetic spectra (250 simulations), shown in Fig. 9. The dashed line indicates the minimum standard deviation attainable for the particular LUTs being used, assuming an even split of best-fit simulations between the nearest over- and underpredictions for all simulations performed. In this particular LUT, the nearest mole fractions to the actual value of 0.05 are 0.049655 and 0.050345, resulting in a minimum value of $\sigma = 3.45 \times 10^{-4}$. The synthetic spectra for this plot use a baseline frequency modulation of $f = 1$ Hz, a fixed noise amplitude of 10%, and a frequency modulation amplitude of 5% of the peak voltage of the ramp. The signal noise and phase of the baseline modulation change for each simulation.

A value of $\Delta\nu = 0$ cm^{-1} corresponds to only using peak points. The standard deviation is high for smaller wavenumber ranges and decreases until leveling off at larger ranges. The smallest possible wavenumber range when the standard deviation has leveled off ($\Delta\nu = 0.03$ cm^{-1}) is chosen for data analysis in this study. This ensures that both the noise is sufficiently averaged and that the least amount of data is used while providing an accurate fit. Similar results are obtained for different levels of baseline modulation and modulation amplitude. When noise levels in the raw data are low, smaller wavenumber ranges can be used.

3. Corrected Baseline: Fitting Function

For real data sets, obtaining a purely linear baseline is difficult. Figure 10 shows four voltage ramps using different levels of baseline frequency modulation ($f = 0$ Hz, 1 Hz, 2 Hz, and 3 Hz). These can be visually compared to the actual ramps taken with parallel-faced optics in the beam path (Fig. 5). The data sets are shifted vertically to separate them for ease of viewing, and a characteristic linear baseline is added (dashed black) to show the deviation from the ideal linear ramp. The phase of the baseline modulation is arbitrary, and different for each of the three modulated sets. Each simulation uses the same gas parameters, with a fixed noise amplitude of 10% and a frequency modulation amplitude of 5% of the peak voltage of the ramp.

Five fits are compared using the standard deviation of the best fits for X_{CO_2} : linear, second-order polynomial, third-order

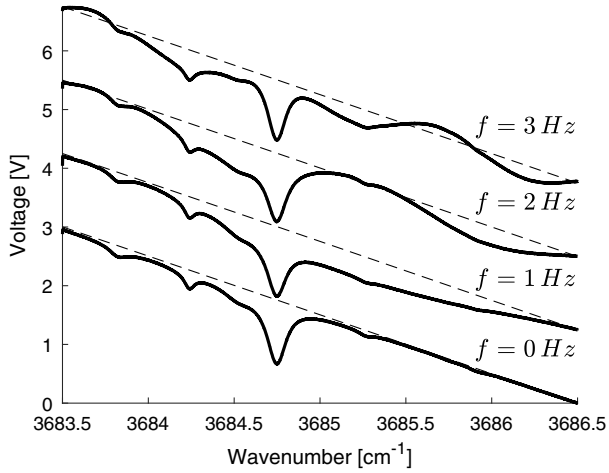

Fig. 10. Baseline frequency modulation for 0 Hz, 1 Hz, 2 Hz, and 3 Hz.

polynomial, second-order Fourier series, and third-order Fourier series. The resulting points for X_{CO_2} are shown in Fig. 11. The X_{H_2O} results are omitted because they show the same trend as the X_{CO_2} data.

It is assumed for this plot that the mean value of the best fits after 50 simulations lies exactly at the actual X_{CO_2} value, although this is not true when the fitting method becomes inadequate at higher frequencies. The LUTs used for these simulations range from 0.04 to 0.06 to increase the resolution of the results, so the maximum standard deviation that can be reached is 0.01. When the best-fit standard deviations reach a value of 0.01, it is the maximum capable for the current LUTs, and the actual fits would be worse if the LUTs were extended further. Similar to the simulations from the previous section, the minimum standard deviation for this LUT is $\sigma = 3.45 \times 10^{-4}$.

For the frequency of 0 Hz (synthetic linear baseline), all the fits perform nominally the same. As the frequency of the synthetic baseline increases, the progressively higher-order fits perform better because they are able to fit the frequency components of the baseline more accurately. At the highest frequency shown here ($f = 3$ Hz), the only adequate fit is the third-order Fourier series. This fit works for the entire range of studied baseline frequencies.

The primary downside of the most inclusive third-order Fourier series fit is that it takes longer computationally than the simpler polynomial fits. If the baseline looks well behaved with only slight etaloning, a second- or third-order polynomial can safely be used. If, however, the baseline appears to have higher-frequency components, the third-order Fourier series is the most conservative choice.

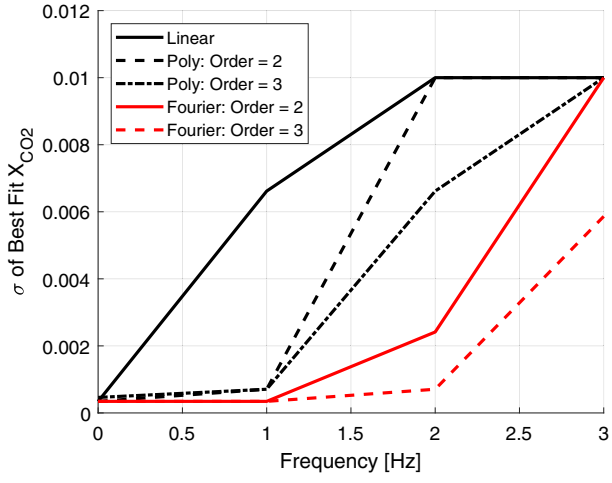

Fig. 11. Standard deviation of best-fit mole fraction for various baseline fitting functions.

B. Heated Test Cell

A heated static test cell [Fig. 1(b)] is used to validate the method with a gas of known concentration at varying temperatures, and to compare to WMS data measurements. The test cell is constructed from aluminum and heated with a 418 W rope heater. Sapphire wedged windows with an antireflection coating provide optical access through the cell. Three thermocouples are located along the length of the 15.24 cm cell to monitor the temperature distribution and provide feedback for the rope heater controller, while a pressure gauge monitors the gas pressure. A gas inlet and gas outlet port are used to introduce the test gas into the cell at the desired pressure. Gas temperatures in this study range between 294 and 533 K, and pressure is 1 atm.

The test cell is placed between the nitrogen-purged pitch and catch boxes. Connecting tubes are used to offset the cell from the acrylic boxes to keep them from melting, and nitrogen is constantly fed into the boxes during the tests in order to maintain a positive pressure and to keep the components cool. The test gas composition is 1% CO_2 with an N_2 balance.

Figure 12 shows the best-fit values for the test gas X_{CO_2} for varying temperatures, where DAS data are plotted with black squares and WMS with red circles. The black dashed lines show ±4% of the actual X_{CO_2} values. The DAS and WMS results agree with each other to within 1%. The results of using DAS with the uncorrected baseline method (blue crosses) always underpredict the actual test gas concentration by approximately

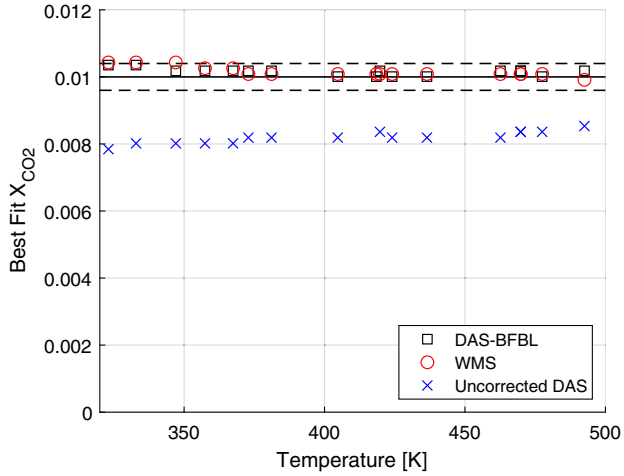

Fig. 12. Best-fit values of X_{CO_2} and X_{H_2O} for the heated test cell test gas, using DAS-BFBL (black squares), WMS (red circles), and uncorrected DAS (blue crosses). Dashed lines are ±4% of test gas concentration.

20%. As feature blending increases, the underprediction will become more pronounced.

C. Biomass Combustion System

The BFBL fitting technique is used to determine the flue exhaust gas composition of X_{CO_2} and X_{H_2O} from the exit of a batch-run, two-stage wood-fired hydronic heater (which will be called a "boiler" for brevity, although at no point in the system is the water boiling) [46]. Both DAS and WMS measurements are obtained, and the results from these measurements are compared to the concentrations using a Testo gas analyzer. WMS measurements provide a second method of validation of the DAS analysis technique in addition to the comparison to boiler gas analyzer diagnostics.

The laser beam path traverses the boiler flue duct where wedged, antireflection coated sapphire windows provide optical access. All combustion and mixing has occurred at this point in the system, and the gases are assumed to be homogeneous across the absorbing path length. The temperature of the absorbing gases is measured using a thermocouple just above the beam path. The absorbing path length is precisely known from the window separation of the specially designed flue duct caps. The pressure is assumed to be 1 atm in the flue, and any slight deviations from this are small enough to be neglected. Using both the DAS-BFBL fitting and the WMS data, the X_{CO_2} and X_{H_2O} are obtained as a function of time. The results from the laser analysis are compared to the gas analyzer measurements of the boiler, which are detailed in Richter *et al.* [47].

Figures 13 and 14 show the comparisons for X_{CO_2} and X_{H_2O}, respectively. For both plots, the solid gray line is the data from the gas analyzer, the black squares are the BFBL fit DAS data, the red circles are the WMS data, and the blue squares are the uncorrected baseline DAS results. The spectra from the start of the run to the end are blended to various extents. Early and late in the run, when temperatures and concentrations are low, the spectra are less blended than during the hot, high-concentration periods in the middle of the run. The extent of blending is indicated with the capped error bars. The uncorrected DAS results always underpredict the actual

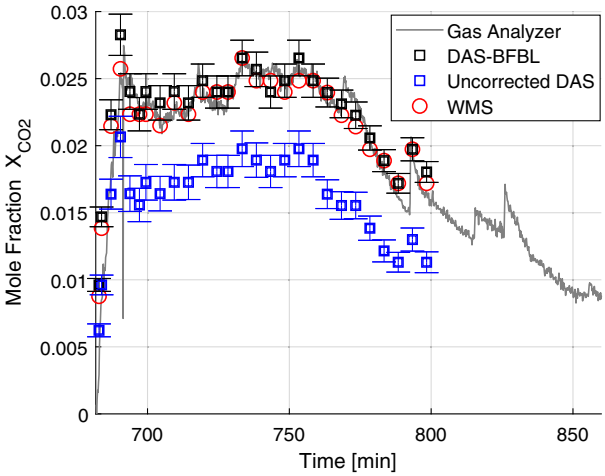

Fig. 13. Typical boiler run flue emissions X_{CO_2} with boiler data (gray line), DAS-BFBL (black squares), uncorrected DAS (blue squares), and WMS (red circles) best-fit data shown.

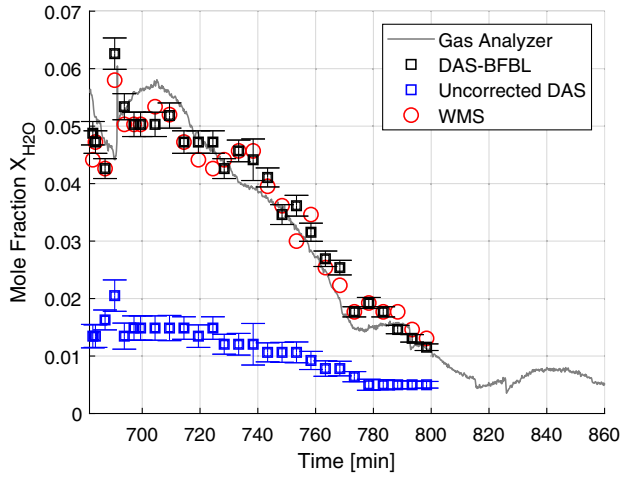

Fig. 14. Typical boiler run flue emissions X_{H_2O} with boiler data (gray line), DAS-BFBL (black squares), uncorrected DAS (blue squares), and WMS (red circles) best-fit data shown.

X_{CO_2} and X_{H_2O} results and provide a poor measurement of the actual gas concentrations. The percent difference between the DAS-BFBL and WMS for CO_2 and H_2O is 2.8% and 5.8%, respectively. The difference between these two values can be attributed in part to the influence each specie has on the total spectrum; it is harder to fit the weaker absorption of the H_2O relative to the strong absorption of the CO_2. Changing the weighting factor in the SSE equation to give more influence to the H_2O features can improve the fit and can be investigated on a case-by-case basis.

The number of peaks present in the transmission data depends on a number of factors: how wide the scan range is, how many absorption features are present, and the FWHM of the features. In contrast to isolated feature DAS, it is better to have closely spaced features that provide more anchoring points for the baseline fitting. Throughout the boiler run duration, five to six distinct peak transmission locations are available for fitting. Using these anchor points provides measurements that agree well with the gas analyzer trends, indicating that the method is useful for measuring gas emissions for varying levels of feature blending.

5. CONCLUSIONS

A novel method for fitting the nonabsorbing baseline for an absorption spectrum with fully blended absorption features is demonstrated. The method is useful for DAS measurements, which can be used when low cost, simplicity, and directness of analysis/results are required. The fitting technique is particularly useful for initial estimates of concentrations of absorbing gases when a nonabsorbing baseline is not present in the absorption spectrum. The BFBL fitting was first tested and refined using synthetically created data. The method uses peak transmission values between absorption features to anchor the nonabsorbing baseline. The baseline is estimated using these points by setting their voltages to the value needed to exactly back out the transmission of the data set at those peak wavenumbers. As raw data noise levels increase, wavenumber ranges

about the peaks' points are used to create the baseline. Etaloning of the raw data is commonplace for absorption measurements, as the laser beam generally passes through non-wedged, parallel-faced optics. While every care can be taken to avoid parallel-faced optics, it cannot be guaranteed, and causes a low-order nonlinearity of the baseline signal. Using a third-order Fourier series for the baseline fitting technique consistently results in the best results.

The baseline fitting technique was validated using a static heated test cell with known test gas concentration of $X_{CO_2} = 1\%$ (N_2 balance). WMS results were also compared to show that it could also be used as a validation for the direct absorption measurements when the gases of interest are not known beforehand. The BFBL fitting was then applied to a wood-fired two-stage hydronic heater to simultaneously measure the flue gas concentrations of X_{CO_2} and X_{H_2O}. Good agreement was found with both the wavelength modulation results and concentrations from the gas analyzer-based analysis of the boiler system. Since the flue gas is at nearly atmospheric pressure for the entirety of the run, the features are not very strongly blended, as they would be for higher-pressure applications. Further study is needed at higher pressures to find the method's upper limitations.

These results indicate that this technique can be useful for measurements with multiple overlapping absorption features either due to pressure broadening or closely spaced species in the scan range. By allowing overlapping features and multiple species in a single scan, fewer lasers can be used in the study of multiple species (such as CO_2 and H_2O), reducing system cost and analysis complexity and interpretation.

Funding. National Science Foundation (NSF) (170447); U.S. Army (W911QY-18-P-0004).

REFERENCES

1. R. K. Hanson, "Applications of quantitative laser sensors to kinetics, propulsion and practical energy systems," Proc. Combust. Inst. **33**, 1–40 (2011).
2. M. Bolshov, Y. Kuritsyn, and Y. Romanovskii, "Tunable diode laser spectroscopy as a technique for combustion diagnostics," Spectrochim. Acta B **106**, 45–66 (2015).
3. C. S. Goldenstein, R. Spearrin, J. B. Jeffries, and R. K. Hanson, "Infrared laser-absorption sensing for combustion gases," Prog. Energy Combust. Sci. **60**, 132–176 (2017).
4. M. E. Webber, J. Wang, S. T. Sanders, D. S. Baer, and R. K. Hanson, "In situ combustion measurements of CO, CO_2, H_2O and temperature using diode laser absorption sensors," Proc. Combust. Inst. **28**, 407–413 (2000).
5. S. T. Sanders, D. W. Mattison, J. B. Jeffries, and R. K. Hanson, "Rapid temperature tuning of a 1.4-μm diode laser with application to high-pressure H_2O absorption spectroscopy," Opt. Lett. **26**, 1568–1570 (2001).
6. T. Le Barbu, B. Parvitte, V. Zeninari, I. Vinogradov, O. Korablev, and G. Durry, "Diode laser spectroscopy of H_2O and CO_2 in the 1.877-μm region for the in situ monitoring of the Martian atmosphere," Appl. Phys. B **82**, 133–140 (2006).
7. G. Durry, L. Joly, T. Le Barbu, B. Parvitte, and V. Zéninari, "Laser diode spectroscopy of the H_2O isotopologues in the 2.64 μm region for the in situ monitoring of the Martian atmosphere," Infrared Phys. Technol. **51**, 229–235 (2008).
8. L. A. Kranendonk, A. W. Caswell, C. L. Hagen, C. T. Neuroth, D. T. Shouse, J. R. Gord, and S. T. Sanders, "Temperature measurements in a gas-turbine-combustor sector rig using swept-wavelength absorption spectroscopy," J. Propul. Power **25**, 859–863 (2009).
9. C. D. Lindstrom, K. R. Jackson, S. Williams, R. Givens, W. F. Bailey, C.-J. Tam, and W. F. Terry, "Shock-train structure resolved with absorption spectroscopy part 1: system design and validation," AIAA J. **47**, 2368–2378 (2009).
10. G. Durry, J. S. Li, I. Vinogradov, A. Titov, L. Joly, J. Cousin, T. Decarpenterie, N. Amarouche, X. Liu, B. Parvitte, O. Korablev, M. Gerasimov, and V. Zéninari, "Near infrared diode laser spectroscopy of C_2H_2, H_2O, CO_2 and their isotopologues and the application to TDLAS, a tunable diode laser spectrometer for the martian PHOBOS-GRUNT space mission," Appl. Phys. B **99**, 339–351 (2010).
11. A. Sepman, Y. Ögren, M. Gullberg, and H. Wiinikka, "Development of TDLAS sensor for diagnostics of CO, HO and soot concentrations in reactor core of pilot-scale gasifier," Appl. Phys. B **122**, 1–12 (2016).
12. J. A. Nwaboh, S. Pratzler, O. Werhahn, and V. Ebert, "Tunable diode laser absorption spectroscopy sensor for calibration free humidity measurements in pure methane and low CO_2 natural gas," Appl. Spectrosc. **71**, 888–900 (2017).
13. R. M. Mihalcea, D. S. Baer, and R. K. Hanson, "A diode-laser absorption sensor system for combustion emission measurements," Meas. Sci. Technol. **9**, 327–338 (1998).
14. R. Mihalcea, M. Webber, D. Baer, R. Hanson, G. Feller, and W. Chapman, "Diode-laser absorption measurements of CO_2, H_2O, N_2O, and NH_3 near 2.0 μm," Appl. Phys. B **67**, 283–288 (1998).
15. A. Farooq, J. Jeffries, and R. Hanson, "CO_2 concentration and temperature sensor for combustion gases using diode-laser absorption near 2.7 μm," Appl. Phys. B **90**, 619–628 (2008).
16. J. M. Meyers and D. Fletcher, "Diode laser absorption sensor design and qualification for CO_2 hypersonic flows," J. Thermophys. Heat Transfer **25**, 193–200 (2011).
17. J. A. Nwaboh, O. Werhahn, P. Ortwein, D. Schiel, and V. Ebert, "Laser-spectrometric gas analysis: CO_2—TDLAS at 2 μm," Meas. Sci. Technol. **24**, 015202 (2013).
18. A. Pogány, O. Ott, O. Werhahn, and V. Ebert, "Towards traceability in CO_2 line strength measurements by TDLAS at 2.7 μm," J. Quantum Spectrosc. Radiat. Transfer **130**, 147–157 (2013).
19. A. Hartmann, R. Strzoda, R. Schrobenhauser, and R. Weigel, "CO sensor for mainstream capnography based on TDLAS," Appl. Phys. B **116**, 1023–1026 (2014).
20. R. M. Spearrin, C. S. Goldenstein, I. A. Schultz, J. B. Jeffries, and R. K. Hanson, "Simultaneous sensing of temperature, CO, and CO_2 in a scramjet combustor using quantum cascade laser absorption spectroscopy," Appl. Phys. B **117**, 689–698 (2014).
21. K. Wu, F. Li, X. Cheng, Y. Yang, X. Lin, and Y. Xia, "Sensitive detection of CO_2 concentration and temperature for hot gases using quantum-cascade laser absorption spectroscopy near 4.2 μm," Appl. Phys. B **117**, 659–666 (2014).
22. J. Chen, C. Li, M. Zhou, J. Liu, R. Kan, and Z. Xu, "Measurement of CO_2 concentration at high-temperature based on tunable diode laser absorption spectroscopy," Infrared Phys. Technol. **80**, 131–137 (2017).
23. A. Hänsel, A. Reyes-Reyes, S. T. Persijn, H. P. Urbach, and N. Bhattacharya, "Temperature measurement using frequency comb absorption spectroscopy of CO_2," Rev. Sci. Instrum. **88**, 053113 (2017).
24. T. Le Barbu, I. Vinogradov, G. Durry, O. Korablev, E. Chassefière, and J.-L. Bertaux, "TDLAS a laser diode sensor for the in situ monitoring of H_2O, CO_2 and their isotopes in the Martian atmosphere," Adv. Space Res. **38**, 718–725 (2006).
25. J. M. Meyers, S. Paris, and D. G. Fletcher, "Development of diode laser absorption instrument for free stream measurements in hypervelocity CO_2 flows," in *26th AIAA Aerodynamic Measurement Technology and Ground Testing Conference* (American Institute of Aeronautics and Astronautics, 2008).
26. A. Farooq, J. Jeffries, and R. Hanson, "High-pressure measurements of CO_2 absorption near 2.7 μm: line mixing and finite duration collision effects," J. Quantum Spectrosc. Radiat. Transfer **111**, 949–960 (2010).
27. S. Gersen, M. van Essen, P. Visser, M. Ahmad, A. Mokhov, A. Sepman, R. Alberts, A. Douma, and H. Levinsky, "Detection of H_2S, SO_2 and NO_2 in CO_2 at pressures ranging from 1–40 bar by using

broadband absorption spectroscopy in the UV/VIS range," Energy Procedia **63**, 2570–2582 (2014).
28. J. Liu, J. Jeffries, and R. Hanson, "Wavelength modulation absorption spectroscopy with 2f detection using multiplexed diode lasers for rapid temperature measurements in gaseous flows," Appl. Phys. B **78**, 503–511 (2004).
29. X. Zhou, J. Jeffries, and R. Hanson, "Development of a fast temperature sensor for combustion gases using a single tunable diode laser," Appl. Phys. B **81**, 711–722 (2005).
30. H. Li, G. B. Rieker, X. Liu, J. B. Jeffries, and R. K. Hanson, "Extension of wavelength-modulation spectroscopy to large modulation depth for diode laser absorption measurements in high-pressure gases," Appl. Opt. **45**, 1052–1061 (2006).
31. A. Farooq, J. B. Jeffries, and R. K. Hanson, "Sensitive detection of temperature behind reflected shock waves using wavelength modulation spectroscopy of CO_2 near 2.7 μm," Appl. Phys. B **96**, 161–173 (2009).
32. A. J. McGettrick, W. Johnstone, R. Cunningham, and J. D. Black, "Tunable diode laser spectroscopy with wavelength modulation: calibration-free measurement of gas compositions at elevated temperatures and varying pressure," J. Lightwave Technol. **27**, 3150–3161 (2009).
33. G. B. Rieker, J. B. Jeffries, and R. K. Hanson, "Calibration-free wavelength-modulation spectroscopy for measurements of gas temperature and concentration in harsh environments," Appl. Opt. **48**, 5546–5560 (2009).
34. R. Sur, T. J. Boucher, M. W. Renfro, and B. M. Cetegen, "Technique of laser calibration for wavelength-modulation spectroscopy with application to proton exchange membrane fuel cell measurements," Appl. Opt. **49**, 61–70 (2010).
35. C. S. Goldenstein, I. A. Schultz, J. B. Jeffries, and R. K. Hanson, "Two-color absorption spectroscopy strategy for measuring the column density and path average temperature of the absorbing species in nonuniform gases," Appl. Opt. **52**, 7950–7962 (2013).
36. K. Sun, X. Chao, R. Sur, C. S. Goldenstein, J. B. Jeffries, and R. K. Hanson, "Analysis of calibration-free wavelength-scanned wavelength modulation spectroscopy for practical gas sensing using tunable diode lasers," Meas. Sci. Technol. **24**, 125203 (2013).
37. A. Klein, O. Witzel, and V. Ebert, "Rapid, time-division multiplexed, direct absorption- and wavelength modulation-spectroscopy," Sensors **14**, 21497–21513 (2014).
38. K. Sun, R. Sur, J. B. Jeffries, R. K. Hanson, T. Clark, J. Anthony, S. Machovec, and J. Northington, "Application of wavelength-scanned wavelength-modulation spectroscopy H_2O absorption measurements in an engineering-scale high-pressure coal gasifier," Appl. Phys. B **117**, 411–421 (2014).
39. C. S. Goldenstein, C. L. Strand, I. A. Schultz, K. Sun, J. B. Jeffries, and R. K. Hanson, "Fitting of calibration-free scanned-wavelength-modulation spectroscopy spectra for determination of gas properties and absorption lineshapes," Appl. Opt. **53**, 356–367 (2014).
40. C. S. Goldenstein, R. M. Spearrin, I. A. Schultz, J. B. Jeffries, and R. K. Hanson, "Wavelength-modulation spectroscopy near 1.4 μm for measurements of H_2O and temperature in high-pressure and -temperature gases," Meas. Sci. Technol. **25**, 055101 (2014).
41. T. R. S. Hayden and G. B. Rieker, "Large amplitude wavelength modulation spectroscopy for sensitive measurements of broad absorbers," Opt. Express **24**, 27910–27921 (2016).
42. R. Vallon, J. Soutade, J.-L. Vérant, J. Meyers, S. Paris, and A. Mohamed, "A compact tunable diode laser absorption spectrometer to monitor CO_2 at 2.7 μm wavelength in hypersonic flows," Sensors **10**, 6081–6091 (2010).
43. J. Reid and D. Labrie, "Second-harmonic detection with tunable diode lasers—comparison of experiment and theory," Appl. Phys. B **26**, 203–210 (1981).
44. I. Gordon, L. Rothman, C. Hill, R. Kochanov, Y. Tan, P. Bernath, M. Birk, V. Boudon, A. Campargue, K. Chance, B. Drouin, J.-M. Flaud, R. Gamache, J. Hodges, D. Jacquemart, V. Perevalov, A. Perrin, K. Shine, M.-A. Smith, J. Tennyson, G. Toon, H. Tran, V. Tyuterev, A. Barbe, A. Császár, V. Devi, T. Furtenbacher, J. Harrison, J.-M. Hartmann, A. Jolly, T. Johnson, T. Karman, I. Kleiner, A. Kyuberis, J. Loos, O. Lyulin, S. Massie, S. Mikhailenko, N. Moazzen-Ahmadi, H. Müller, O. Naumenko, A. Nikitin, O. Polyansky, M. Rey, M. Rotger, S. Sharpe, K. Sung, E. Starikova, S. Tashkun, J. V. Auwera, G. Wagner, J. Wilzewski, P. Wcislo, S. Yu, and E. Zak, "The HITRAN2016 molecular spectroscopic database," J. Quantum Spectrosc. Radiat. Transfer **203**, 3–69 (2017).
45. A. McLean, C. Mitchell, and D. Swanston, "Implementation of an efficient analytical approximation to the Voigt function for photoemission lineshape analysis," J. Electron Spectrosc. Relat. Phenom. **69**, 125–132 (1994).
46. J. P. Richter, B. T. Bojko, J. C. Mollendorf, and P. E. DesJardin, "Measurements of fuel burn rate, emissions and thermal efficiency from a domestic two-stage wood-fired hydronic heater," Renew. Energy **96**, 400–409 (2016).
47. J. P. Richter, J. M. Weisberger, J. C. Mollendorf, and P. E. DesJardin, "Emissions from a domestic two-stage wood-fired hydronic heater: effects of non-homogeneous fuel decomposition," Renew. Energy **112**, 187–196 (2017).